Optimizing the Mechanical Properties of Carbon Nanotube-Reinforced Metal Matrix Composites: A Comparative Study of Finite Element and Semi-Empirical Approaches

Elkhawad Ali Elfaki
Mechanical Engineering Department, University of Bisha, Bisha, Saudi Arabia
aahmed@ub.edu.sa (corresponding author)

Received: 20 August 2025 | Revised: 20 September 2025 | Accepted: 6 October 2025

 DOI: https://doi.org/10.48084/etasr.14195

ABSTRACT

This study analyzes the mechanical properties of Carbon Nanotube (CNT)-reinforced Metal Matrix Composites (MMCs) using a novel integration of Finite Element Analysis (FEA) and semi-empirical modeling, in order to evaluate the influence of CNT chirality, volume fractions, and lengths on longitudinal, transverse, and shear moduli, through a three-dimensional Representative Volume Element (RVE). The results reveal significant stiffness improvements of up to 76% for aluminum-based composites, especially those containing zigzag CNTs. A comparative analysis between FEA and Halpin-Tsai-based semi-empirical models reveals key modeling assumptions. This work advances the design of high-performance CNT-MMCs for use in the aerospace, automotive, biomedical, and energy sectors.

Keywords-carbon nanotubes; metal matrix composites; finite element analysis; mechanical properties

I. INTRODUCTION

The development of CNT-reinforced MMCs can lead to the manufacture of advanced materials with superior mechanical properties. Despite extensive experimental studies, the relationship between CNT structure, volume fraction, and matrix material properties, is still unclear, with previous works focusing on molecular dynamics simulations or continuum-based models. However, a comprehensive comparative framework that combines FEA and semi-empirical models is insufficiently explored. This study bridges the specific gap by using a new way to combine three-dimensional Finite Element Modeling (FEM) with well-known semi-empirical equations, such as the Halpin-Tsai model and the extended rule of mixtures model, to evaluate the mechanical properties of CNT-MMCs. Unlike previous research, which often assumes homogeneous composite behavior, this study explicitly considers the effects of CNT chirality (i.e., zigzag, armchair, and chiral configurations), volume fraction, and length within aluminum, copper, and iron matrix materials. The chiral indices (m, n) determine the structural arrangement of carbon atoms in the CNT lattice. Zigzag CNTs (m, 0) have a straight edge along their circumference, and chiral CNTs (m, n, where $m \neq n$) have a helical structure. These configurations significantly impact the mechanical and electronic properties of CNTs. Building on existing research, this study:

- Demonstrates the superior mechanical performance of zigzag CNT configurations under varying matrix conditions.
- Uses semi-empirical models to confirm the FEA method and identify its limitations.
- Proposes practical ways to improve the performance of CNT-reinforced materials.

The findings of this study can be used in many systems: The lightweight nature of CNT-reinforced materials makes them ideal for satellite frames, and turbine blades, increasing fuel efficiency and improving mechanical reliability in difficult conditions, such as space. Drive shafts, brake discs, and body panels, could reduce weight while maintaining or improving durability and safety standards in the car industry. Materials for medical implants, prosthetics, and surgical tools, may provide better compatibility with biological tissues. Furthermore, in renewable energy systems, such as wind turbine blades and photovoltaic systems, can improve performance and longevity. There are two types of fiber reinforcement: continuous and short. Various computational modeling tools have been developed to characterize and analyze nanocomposites. Techniques, such as molecular dynamics simulations, continuum mechanics, the finite element method, and constitutive modeling, have been used to estimate nanoscale properties. CNTs exhibit a Young's modulus in the tera pascal (TPa) range [1], combined with high stiffness. The exceptional properties of CNT composites allow for innovative applications in many fields [2-4]. Empirical models have been used to study the elastic properties of single and multilayered nanotubes, showing that their Young's and shear moduli are comparable to those of diamond [5]. Furthermore, it has been indicated that

the elastic modulus is largely insensitive to nanotube geometry, including size, helicity, and the number of layers. Authors in [2] showed that incorporating 1% by weight of CNTs into a matrix material increased the composite's tensile strength by 25% and its elastic stiffness by 36%-42%. Authors in [6] deployed the short-fiber composite theory and found that adding 1% CNTs by weight achieved the same enhancement in elastic modulus as adding 10% carbon fibers by weight. Authors in [7, 8] developed constitutive models for composite materials reinforced with Single-Walled Carbon Nanotubes (SWCNTs) using an equivalent-continuum modeling technique. These models aimed to determine the constitutive properties of SWCNT/polymer composites with aligned and random nanotube orientations, as well as various lengths and volume fractions. Authors in [9] examined the elastic moduli of polymer-nanotube composites through molecular dynamics simulations, constructing stress-strain curves for composites featuring SWCNTs embedded in a polyethylene matrix using the Parrinello and Rahman approach [10]. Authors in [11-14] analyzed the effective properties of CNT-based composites through continuum mechanics. They obtained significant numerical results regarding the load-carrying capacity of CNTs within a matrix by using a three-dimensional RVE and FEA. The FEM is essential for predicting and simulating the physical behavior of complex engineering systems [15-20], offering a reliable computational framework. It provides approximate solutions to complex engineering problems involving intricate geometries and boundary conditions [21-24]. The adoption of FEA has revolutionized the design and modeling of physical phenomena across various engineering disciplines, significantly improving accuracy, efficiency, and problem-solving capabilities [25-27]. Authors in [28] conducted an in-depth study on how material parameters and constitutive relationships influence the dynamic mechanical response of composite laminated plates under varying impact velocities. Their findings revealed a significant increase in energy absorption as impact velocity increased. Authors in [29] analyzed the properties, applications, and limitations of CNTs, highlighting the risks associated with toxic metals during usage. Authors in [30] explored the synthesis, properties, and applications of CNTs, while authors in [31] examined the mechanical properties and aerospace applications of CNTs. This study uses a 3D FEM framework to examine the mechanical behavior of short CNT-MMCs, which allows for a detailed analysis of how CNT structure, volume fraction, length, and interface properties affect the performance [32, 33]. This work identifies composite configurations that significantly increase stiffness, providing valuable insights for MMC design optimization.

II. THEORETICAL BACKGROUND OF FINITE ELEMENT ANALYSIS

The physical properties of short fiber composites can be predicted using the stress distribution obtained through FEA. Both the matrix and the CNTs in an RVE are considered to be continuous, linearly elastic, isotropic, and homogeneous materials with known Young's modulus, shear modulus, and Poisson's ratio. Furthermore, the CNTs are bonded to the matrix at the interface. Thus, the CNT-based MMC has three effective material constants that must be determined: the longitudinal (E_L), transverse (E_T), and shear (G) moduli. In the case of short CNTs fully located inside the RVE, a solid square RVE can be used to determine the composite constants; otherwise, it is difficult to find elasticity solutions. For a transversely isotropic material, Hooke's law stress-strain relationships are [34]:

$$\begin{pmatrix}\sigma_x\\ \sigma_y\\ \sigma_z\\ \tau_{xy}\\ \tau_{yz}\\ \tau_{zx}\end{pmatrix} = [C]\begin{pmatrix}\varepsilon_x\\ \varepsilon_y\\ \varepsilon_z\\ \gamma_{xy}\\ \gamma_{yz}\\ \gamma_{zx}\end{pmatrix} \quad (1)$$

$$\begin{pmatrix}\varepsilon_x\\ \varepsilon_y\\ \varepsilon_z\\ \gamma_{xy}\\ \gamma_{yz}\\ \gamma_{zx}\end{pmatrix} = [C]^{-1}\begin{pmatrix}\sigma_x\\ \sigma_y\\ \sigma_z\\ \tau_{xy}\\ \tau_{yz}\\ \tau_{zx}\end{pmatrix} \quad (2)$$

where $[C]$ is the stiffness matrix, and $[C]^{-1}$ is the inverted stiffness matrix, which is given for a transverse isotropic material by:

$$[C]^{-1} = \begin{bmatrix} 1/E & -\frac{v}{E} & -\frac{v}{E} & 0 & 0 & 0 \\ -\frac{v}{E} & 1/E & -\frac{v}{E} & 0 & 0 & 0 \\ -\frac{v}{E} & -\frac{v}{E} & 1/E & 0 & 0 & 0 \\ 0 & 0 & 0 & 1/G & 0 & 0 \\ 0 & 0 & 0 & 0 & 1/G & 0 \\ 0 & 0 & 0 & 0 & 0 & 1/G \end{bmatrix} \quad (3)$$

where v is the Poisson's ratio. The shear modulus, G, is a function of two elastic constants, E and v:

$$G = E / 2(1 - v) \quad (4)$$

For a square RVE with a total longitudinal length of L and a side length a, as shown in Figure 1, the stress and strain components at any point on the lateral surface are: $\sigma_x = \sigma_y = 0$, $\varepsilon_z = \Delta L/L$, and $\varepsilon_x = \varepsilon_y = -\Delta a/a$, where ΔL and Δa are the longitudinal and lateral displacements, respectively.

$$E_z = \sigma_z / \varepsilon_z = (L / \Delta L)\, \sigma_{ave} \quad (5)$$

where σ_{ave} is the average stress on the lateral surface:

$$\sigma_{ave} = (1/A) \int A[\sigma_z(x, y, L/2)]dA = (4/a \times a) \int x \int y[\sigma_z(x, y, L/2)]dxdy \quad (6)$$

where A is the area of the lateral surface and σ_{ave} can be obtained for the RVE from the FEM results. Considering $\varepsilon_x = \varepsilon_y = -\frac{v}{E}\sigma_z = -v\frac{\Delta L}{L} = \frac{\Delta a}{a}$, we have:

$$v = -(\Delta a/a)(L/\Delta L) \quad (7)$$

Once σ_{ave}, ΔL, and Δa are determined, the effective longitudinal Young's modulus E_z and the major Poisson's ratio v can be measured. Using the same analysis with the RVE under a uniform lateral load yields the effective lateral (transverse) Young's modulus, E_x. Consequently, the minor Poisson's ratio (v') is:

$$v' = E_z/E_x \quad (8)$$

The direction in which the graphite sheet is rolled up defines the chirality of CNTs, which are categorized as zigzag, armchair, or chiral. Zigzag CNTs (*m*, 0) and armchair CNTs (*m*, *m*) are special cases. Chiral CNTs (*m*, *n*), on the other hand, have a unique helical arrangement that affects their mechanical response to applied stress.

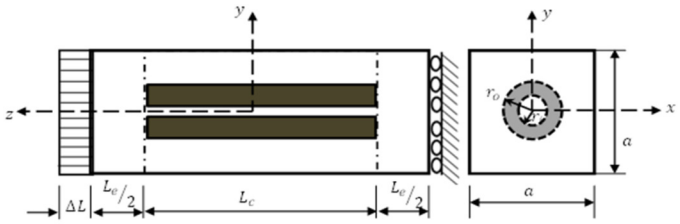

Fig. 1. Visualization of carbon nanotubes within the RVE.

III. FINITE ELEMENT MODELING OF MECHANICAL PROPERTIES

In this study, ANSYS software was used to run simulations with RVE models. Three metal materials—iron, copper, and aluminum—and three types of carbon nanotubes—armchair, zigzag, and chiral—were considered. The carbon nanotubes are treated as short fibers in the RVE. The parameterized ANSYS models were developed using APDL code (script) and were applicable to all cases. FEA was utilized to analyze the mechanical responses of these RVEs under different loading conditions. This research proposes square RVEs for evaluating the effective material properties of CNT-based composites. Figure 1 shows that the square of the RVE is divided into two segments. One segment includes the two ends, which have a total length of L_e and a Young's modulus of E_m. The other segment covers the center part, which has a length of L_{CNT} and an effective Young's modulus of E_c. This simple strength of materials model ignores the two hemispherical end caps of the CNT [32-34]. The direction in which the graphite sheet is rolled to form the nanotube determines its chirality, which affects whether the nanotube is metallic or behaves like a semiconductor. This roll direction is defined by a vector known as the "roll-up vector" or "chiral vector" ($\overrightarrow{Ch}$) and can be expressed as a linear combination of the unit translational vectors in the hexagonal lattice:

$$\overrightarrow{Ch} = m \times a_1 + n \times a_2 \quad (9)$$

where *m* and *n* are integers, while a_1 and a_2 are the hexagonal graphite lattice vectors. The angle between $\overrightarrow{Ch}$ and a_1 is known as the chiral angle, θ, and can be calculated as [34]:

$$\theta = \sin^{-1}\left[\frac{\sqrt{3}m}{2\sqrt{n^2+m^2+nm}}\right] \quad (10)$$

Different types of nanotubes result from variations in the chiral indices (*m*, *n*). In addition to being classified as single-, double-, or multi-walled, nanotubes may have a zigzag (*m* = 0), armchair (*m*, *m*), or chiral (*m*, *n*) configuration. The diameter of any nanotube can be calculated as:

$$d_0 = \frac{a_0\sqrt{(m^2+mn+n^2)}}{\pi} \quad (11)$$

where a_0 is the length (in nm) of vector a_1 (or a_2). The volume fraction of the CNT is given by:

$$V_f = \frac{\pi(r_o^2-r_i^2)}{a^2-\pi r_i^2} \quad (12)$$

where V_f is the CNTvolume, r_o and r_i are the outer and inner radii of CNT, and *a* is the side length (width) of RVE, which is given by:

$$a = \sqrt{\frac{\pi(r_o^2-r_i^2)}{V_f} + \pi r_i^2} \quad (13)$$

The above were used in the MATLAB code to predict the elastic properties of carbon nanotubes treated as short fibers in MMCs. The dimensions of the square RVE and carbon nanotubes used to generate the model geometries are calculated based on (12) and (13) and are presented in Tables I–III. The volume fractions used in this research are 3%, 7%, and 11%, and the length of the square RVE is assumed to be 10 nm.

TABLE I. DIMENSIONS OF SHORT FIBER CNT CONFIGURATIONS AT A VOLUME FRACTION OF 3%

	CNT		*do*	*di*	***a* (width of square RVE)**					
					Case 1		Case 2		Case 3	
	M	*N*			L_{CNT} =3	L_e =7	L_{CNT} =5	L_e =5	L_{CNT} =8	L_e =2
Armchair CNT	5	5	0.848	0.508	3.2105		4.9041		9.8082	
	10	10	1.526	1.186	4.5104		6.8898		13.779	
	15	15	2.204	1.864	5.4837		8.3765		16.753	
Zigzag CNT	5	0	0.561	0.221	2.4438		3.7329		7.4659	
	10	0	0.953	0.613	3.4468		5.2650		10.530	
	15	0	1.344	1.004	4.2054		6.4238		12.847	
Chiral CNT	5	10	1.206	0.866	3.9548		6.0411		12.082	
	10	15	1.876	1.536	5.0406		7.6997		15.399	
	15	20	2.551	2.211	5.9102		9.0280		18.056	

TABLE II. DIMENSIONS OF SHORT FIBER CNT CONFIGURATIONS AT A VOLUME FRACTION OF 7%

	CNT		*do*	*di*	***a* (width of square RVE)**					
					Case 1		Case 2		Case 3	
	M	*N*			L_{CNT} =3	L_e =7	L_{CNT} =5	L_e =5	L_{CNT} =8	L_e =2
Armchair CNT	5	5	0.848	0.508	2.0965		3.2025		6.4049	
	10	10	1.526	1.186	2.9189		4.4588		8.9176	
	15	15	2.204	1.864	3.5122		5.3650		10.730	
Zigzag CNT	5	0	0.561	0.221	1.5997		2.4436		4.8871	
	10	0	0.953	0.613	2.2481		3.4339		6.8679	
	15	0	1.344	1.004	2.7286		4.1680		8.3361	
Chiral CNT	5	10	1.206	0.866	2.5709		3.9272		7.8545	
	10	15	1.876	1.536	3.2450		4.9568		9.9136	
	15	20	2.551	2.211	3.7642		5.7499		11.499	

IV. MECHANICAL PROPERTIES OF CNT REINFORCED COMPOSITE

To compare the FEM results with the rule of mixtures approach, the mechanical properties of a short CNT metal-matrix nanocomposite, were estimated. The Halpin–Tsai equations approximate the longitudinal and transverse moduli of aligned short-fiber composites.

TABLE III. DIMENSIONS OF SHORT FIBER CNT CONFIGURATIONS AT A VOLUME FRACTION OF 11%

	CNT		***do***	***a* (width of square RVE)**					
				Case 1		Case 2		Case 3	
	M	*N*		L_{CNT} =3	L_e =7	L_{CNT} =5	L_e =5	L_{CNT} =8	L_e =2
Armchair CNT	5	5	0.848	1.6683		2.5483		5.0966	
	10	10	1.526	2.3012		3.5152		7.0304	
	15	15	2.204	2.7384		4.1829		8.3659	
Zigzag CNT	5	0	0.561	1.2759		1.9491		3.8982	
	10	0	0.953	1.7866		2.7291		5.4582	
	15	0	1.344	2.1570		3.2949		6.5898	
Chiral CNT	5	10	1.206	2.0364		3.1107		6.2214	
	10	15	1.876	2.5441		3.8862		7.7724	
	15	20	2.551	2.9166		4.4552		8.9105	

The Halpin-Tsai equations for longitudinal (E_L), transverse (E_T), and shear (G) moduli can be written as [34]:

$$E_L = \frac{1+\frac{2\ell}{d}\eta_L V_f}{1-\eta_L V_f} E_m \quad (14)$$

$$E_T = \frac{1+\frac{2\ell}{d}\eta_T V_f}{1-\eta_T V_f} E_m \quad (15)$$

$$\mathrm{G} = \frac{1+\eta_G \mathrm{V_f}}{1+\eta_G \mathrm{V_m}} \times \mathrm{G_m} \quad (16)$$

where $\eta_L = \frac{(E_f/E_m)-1}{(E_f/E_m)+2(\ell/d)}$, $\eta_T = \frac{(E_f/E_m)-1}{(E_f/E_m)+2}$, $\eta_G = \frac{(G_f/G_m)-1}{(G_f/G_m)+1}$, ℓ and d are the fiber length and diameter, respectively, V_f is the volume fraction of CNT, E_f and E_m are the fiber and matrix Young's moduli, while G_f and G_m are their shear moduli, respectively. As an alternative, the longitudinal effective Young's modulus can be obtained by:

$$E_L = E_f V_f + E_m(1 - V_f) \quad (17)$$

Then, considering the compatibility of strains and the equilibrium of stresses, the longitudinal effective Young's modulus for the composite is:

$$E_L = \frac{1}{\frac{1}{\mathrm{E_m}} \times \left(\frac{\mathrm{Le}}{\mathrm{L}}\right) + \frac{1}{\mathrm{E_f}} \times \frac{\mathrm{L_{CNT}}}{\mathrm{L}} \times \frac{\mathrm{A}}{\mathrm{A_{CNT}}}} \quad (18)$$

where L, L_e, and L_{CNT} are the total length of RVE, the length of the two ends, and the length of the CNT, respectively, A is the area of the whole RVE ($A = a^2$), and A_{CNT} is the area of CNT ($\mathrm{A_{CNT}} = \pi(\mathrm{r_o^2} - \mathrm{r_i^2})$). Similarly, the transverse effective Young's modulus and effective shear modulus can be obtained by:

$$\mathrm{E_T} = \frac{(\mathrm{E_f} \times \mathrm{E_m})}{(\mathrm{E_m} \times \mathrm{V_f}) + (\mathrm{E_f} \times \mathrm{V_m})} \quad (19)$$

$$\mathrm{G_T} = \frac{(\mathrm{G_f} \times \mathrm{G_m})}{(\mathrm{G_m} \times \mathrm{V_f}) + (\mathrm{G_f} \times \mathrm{V_m})} \quad (20)$$

These equations have been widely validated and adapted for CNT-based composites, offering an efficient means of estimating mechanical properties under various configurations [34, 35].

V. RESULTS AND DISCUSSION

This study considers the effective material constants of CNT composites, including the longitudinal and transverse Young's moduli, as well as the shear modulus. Three matrix materials—iron, copper, and aluminum—were tested using three volume fraction ratios (3%, 7%, and 11%) and three short CNT lengths (3 nm, 5 nm, and 8 nm). The results of the three effective material constants of the composites relative to the matrix materials (E_c/E_m, G_c/G_m) obtained by FEM are presented and discussed, using empirical equations for comparison. The results are demonstrated in terms of the fiber Young's modulus relative to the matrix Young's modulus (E_f/E_m) as 4.76, 7.69, and 14.29 for iron, copper, and aluminum, respectively.

A. Longitudinal Young Modulus

The FEA results for the longitudinal Young's modulus are presented in Tables IV–VI, showing that the material's longitudinal stiffness increased relative to the matrix material for different fiber lengths, volume fractions, and CNT types. In general, longitudinal stiffness increased with an increase in volume fraction and/or fiber length. Among the CNT structures, zigzag showed the greatest increase in stiffness, while chiral showed the least.

TABLE IV. LONGITUDINAL YOUNG'S MODULUS RATIO (E_C/E_M) FOR E_F/E_M = 4.76

		Armchair (5, 5)			**Zigzag (5, 0)**				**Chiral (5, 10)**		
		L_{CNT} =3	L_{CNT} =5	L_{CNT} =8	L_{CNT} =3	L_{CNT} =5		L_{CNT} =8	L_{CNT} =3	L_{CNT} =5	L_{CNT} =8
Volume fraction (%)	3%	FEA	1.075	1.079	1.085	1.088	1.093	1.099	1.069	1.077	1.084
		(14)	1.078	1.088	1.095	1.086	1.095	1.100	1.070	1.081	1.090
		(18)	1.03	1.05	1.09	1.03	1.05	1.09	1.02	1.05	1.08
	7%	FEA	1.175	1.184	1.200	1.206	1.218	1.231	1.161	1.179	1.196
		(14)	1.184	1.207	1.224	1.203	1.222	1.235	1.166	1.191	1.211
		(18)	1.054	1.106	1.196	1.063	1.113	1.199	1.041	1.097	1.191
	11%	FEA	1.275	1.290	1.313	1.323	1.343	1.363	1.253	1.280	1.308
		(14)	1.293	1.328	1.354	1.322	1.351	1.372	1.265	1.304	1.335
		(18)	1.077	1.156	1.298	1.090	1.167	1.303	1.056	1.141	1.291

The aluminum-based material exhibited greater increase in stiffness than copper and iron. The composite materials tested with a zigzag CNT chiral index of (5, 0), a volume fraction of 11%, and a fiber length of 8 nm exhibited the highest increases in stiffness: 76%, 65%, and 36%, respectively, over the stiffness of their matrix materials (aluminum, copper, and iron). Conversely, composite materials with a chiral CNT structure (5, 10), a volume fraction of 3%, and a fiber length of 3 nm exhibited the lowest increases in stiffness: 7%, 11%, and 17%, respectively, relative to their matrix materials.

TABLE V. LONGITUDINAL YOUNG'S MODULUS RATIO (E_C/E_M) FOR E_F/E_M = 7.69

			Armchair (5, 5)			**Zigzag (5, 0)**			**Chiral (5, 10)**		
			L_{CNT} =3	L_{CNT} =5	L_{CNT} =8	L_{CNT} =3	L_{CNT} =5	L_{CNT} =8	L_{CNT} =3	L_{CNT} =5	L_{CNT} =8
Volume fraction (%)	0.03	FEA	1.127	1.147	1.162	1.148	1.165	1.176	1.108	1.130	1.148
		(14)	1.111	1.133	1.151	1.224	1.149	1.165	1.096	1.118	1.138
		(18)	1.047	1.087	1.153	1.051	1.090	1.154	1.042	1.083	1.151
	0.07	FEA	1.295	1.343	1.379	1.346	1.385	1.412	1.253	1.304	1.347
		(14)	1.265	1.315	1.357	1.536	1.352	1.387	1.229	1.281	1.326
		(18)	1.094	1.180	1.338	1.102	1.187	1.341	1.082	1.171	1.333
	0.11	FEA	1.465	1.539	1.596	1.544	1.605	1.647	1.398	1.478	1.545
		(14)	1.424	1.502	1.566	1.864	1.559	1.613	1.369	1.449	1.519
		(18)	1.128	1.254	1.505	1.140	1.264	1.511	1.109	1.240	1.497

TABLE VI. LONGITUDINAL YOUNG'S MODULUS RATIO (E_C/E_M) FOR E_F/E_M = 14.29

			Armchair (5, 5)			**Zigzag (5, 0)**			**Chiral (5, 10)**		
			L_{CNT} =3	L_{CNT} =5	L_{CNT} =8	L_{CNT} =3	L_{CNT} =5	L_{CNT} =8	L_{CNT} =3	L_{CNT} =5	L_{CNT} =8
Volume fraction (%)	0.03	FEA	1.184	1.193	1.199	1.193	1.201	1.207	1.177	1.186	1.193
		(14)	1.154	1.199	1.242	1.190	1.237	1.277	1.126	1.167	1.209
		(18)	1.088	1.162	1.293	1.092	1.165	1.295	1.084	1.158	1.291
	0.07	FEA	1.430	1.451	1.464	1.451	1.471	1.483	1.413	1.431	1.449
		(14)	1.368	1.473	1.573	1.452	1.561	1.656	1.303	1.399	1.498
		(18)	1.159	1.308	1.899	1.090	1.315	1.903	1.069	1.300	1.893
	0.11	FEA	1.676	1.710	1.730	1.710	1.741	1.760	1.649	1.679	1.706
		(14)	1.593	1.759	1.916	1.727	1.898	2.043	1.491	1.643	1.799
		(18)	1.203	1.409	1.895	1.212	1.418	1.902	1.188	1.396	1.887

Tables IV-VI present the increases in longitudinal stiffness obtained for the tested composites using the Halpin-Tsai semi-empirical (14) and the extended rule of mixture (18) equations. The results from the Halpin-Tsai are higher than those from the extended rule of mixture. The difference increases as the volume fraction increases, the fiber length decreases, and the Young's modulus of the matrix material increases. This difference is also affected by the type of CNT. The FEA results are comparable to the numerical results of the two equations. Table VII shows the ranges of increase in the longitudinal stiffness of the effective composite materials obtained by FEA and the documented numerical equations.

TABLE VII. RANGES OF PERCENTAGE INCREASE IN LONGITUDINAL STIFFNESS FOR THE DIFFERENT MODELS

E_f/E_m	**FEA**	**(14)**	**(18)**
4.76	7% - 36%	7% - 37%	2% - 30%
7.69	11% - 65%	10% -86%	4% - 51%
14.29	17% - 76%	13% - 104%	7% - 90%

Figure 2 shows the percentage increase ranges for FEA, (14), and (18) at different E_f/E_m values. FEA (blue) shows steadily increasing ranges with E_f/E_m, from 7%–36% at 4.76 to 17%–76% at 14.29. Furthermore, (14) (green) closely tracks FEA at lower ratios, but it predicts higher maximum values and reaches over 100% at E_f/E_m = 14.29, while (18) (red) starts from a lower baseline (2%–30% at E_f/E_m = 4.76) but rises sharply to 7%–90% at E_f/E_m = 14.29, indicating broader variability. The FEA results lie between the two, providing conservative yet consistent estimates. The variations observed between FEA results and semi-empirical models, such as the Halpin-Tsai equations and the extended rule of mixtures, arise from the inherent assumptions and limitations of each approach. The FEA method provides a detailed analysis by accounting for localized interactions, such as CNT-matrix bonding and nonlinear stress distributions, which are often oversimplified or neglected in semi-empirical models. Additionally, the influence of CNT chirality and orientation, which is explicitly captured in FEA, is not fully represented in semi-empirical equations. When combined with CNT reinforcement, these materials could potentially yield improved stiffness-to-weight ratios, further enhancing their suitability for high-performance applications.

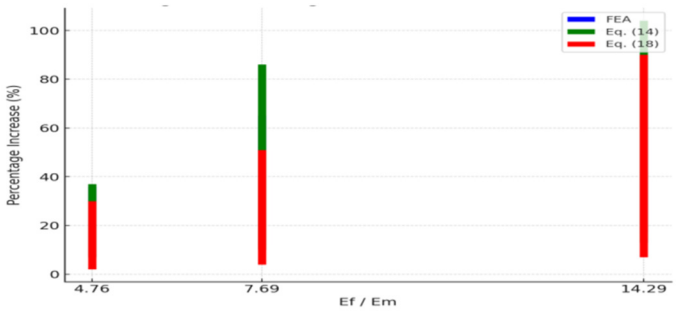

Fig. 2. Ranges of Percentage increase for different models.

B. *Transvers Young's Modulus*

The FEA results for the transverse Young's modulus are shown in Tables VIII-X for three fiber-to-matrix modulus ratios (E_c/E_m): 4.76, 7.69, and 14.29. For each ratio, the transverse stiffness of the composite material increases relative to the matrix material. The behavior of transverse stiffness in relation to changes in fiber length and volume fraction is similar to that of longitudinal stiffness, but with lower values. Similar behavior is observed with different CNT structures and matrix materials. The highest increases in transverse stiffness are shown for L_{CNT} = 8 nm, V_f = 11%, and a zigzag structure, for each matrix material tested. The lowest values are shown for L_{CNT} = 3 nm, V_f = 3%, and a chiral structure.

TABLE VIII. TRANSVERSE YOUNG'S MODULUS RATIO (E_C/E_M) FOR E_F/E_M = 4.76

			Armchair (5, 5)			**Zigzag (5, 0)**			**Chiral (5, 10)**		
			L_{CNT} =3	L_{CNT} =5	L_{CNT} =8	L_{CNT} =3	L_{CNT} =5	L_{CNT} =8	L_{CNT} =3	L_{CNT} =5	L_{CNT} =8
Volume fraction (%)	3%	FEA	1.024	1.030	1.035	1.030	1.041	1.043	1.020	1.020	1.024
		(19)	1.024	1.024	1.024	1.024	1.024	1.024	1.024	1.024	1.024
		(15)	1.051	1.051	1.051	1.051	1.051	1.051	1.051	1.051	1.051
	7%	FEA	1.038	1.043	1.047	1.043	1.047	1.050	1.033	1.038	1.040
		(19)	1.059	1.059	1.059	1.059	1.059	1.059	1.059	1.059	1.059
		(15)	1.122	1.122	1.122	1.122	1.122	1.122	1.122	1.122	1.122
	11%	FEA	1.050	1.060	1.064	1.060	1.068	1.071	1.045	1.055	1.057
		(19)	1.095	1.095	1.095	1.095	1.095	1.095	1.095	1.095	1.095
		(15)	1.196	1.196	1.196	1.196	1.196	1.196	1.196	1.196	1.196

TABLE IX. TRANSVERSE YOUNG'S MODULUS RATIO (E_C/E_M) FOR E_F/E_M = 7.69

			Armchair (5, 5)			**Zigzag (5, 0)**			**Chiral (5, 10)**		
			L_{CNT} =3	L_{CNT} =5	L_{CNT} =8	L_{CNT} =3	L_{CNT} =5	L_{CNT} =8	L_{CNT} =3	L_{CNT} =5	L_{CNT} =8
Volume fraction (%)	3%	FEA	1.029	1.034	1.040	1.037	1.042	1.049	1.021	1.031	1.037
		(19)	1.027	1.027	1.027	1.027	1.027	1.027	1.027	1.027	1.027
		(15)	1.051	1.051	1.051	1.051	1.051	1.051	1.051	1.051	1.051
	7%	FEA	1.037	1.051	1.057	1.048	1.058	1.064	1.031	1.042	1.052
		(19)	1.065	1.065	1.065	1.065	1.065	1.065	1.065	1.065	1.065
		(15)	1.122	1.122	1.122	1.122	1.122	1.122	1.122	1.122	1.122
	11%	FEA	1.062	1.075	1.082	1.075	1.083	1.088	1.050	1.057	1.066
		(19)	1.106	1.106	1.106	1.106	1.106	1.106	1.106	1.106	1.106
		(15)	1.196	1.196	1.196	1.196	1.196	1.196	1.196	1.196	1.196

TABLE X. TRANSVERSE YOUNG'S MODULUS RATIO (E_C/E_M) FOR E_F/E_M = 14.29

			Armchair (5, 5)			**Zigzag (5, 0)**			**Chiral (5, 10)**		
			L_{CNT} =3	L_{CNT} =5	L_{CNT} =8	L_{CNT} =3	L_{CNT} =5	L_{CNT} =8	L_{CNT} =3	L_{CNT} =5	L_{CNT} =8
Volume fraction (%)	3%	FEA	1.052	1.063	1.072	1.057	1.070	1.079	1.049	1.059	1.066
		(19)	1.029	1.029	1.029	1.029	1.029	1.029	1.029	1.029	1.029
		(15)	1.051	1.051	1.051	1.051	1.051	1.051	1.051	1.051	1.051
	7%	FEA	1.067	1.074	1.086	1.080	1.083	1.099	1.059	1.069	1.076
		(19)	1.070	1.070	1.070	1.070	1.070	1.070	1.070	1.070	1.070
		(15)	1.122	1.122	1.122	1.122	1.122	1.122	1.122	1.122	1.122
	11%	FEA	1.086	1.089	1.103	1.090	1.094	1.107	1.079	1.083	1.089
		(19)	1.114	1.114	1.114	1.114	1.114	1.114	1.114	1.114	1.114
		(15)	1.196	1.196	1.196	1.196	1.196	1.196	1.196	1.196	1.196

Tables VIII-X also present the computed results for the transverse properties, which were obtained using the Halpin-Tsai equation (15) and the extended rule of mixture equation (19). These equations depend only on the volume fraction and the Young's moduli of the fiber and matrix, and not on fiber length and CNT structure. The Halpin-Tsai results exhibit higher values compared to the extended rule of mixture equation, along with the longitudinal stiffness. In general, the FEA results are comparable to the computed results obtained using these equations. Table XI shows the ranges of the increase in transverse stiffness of effective composite materials obtained by FEA and documented numerical expressions. For the transverse modulus, the observed deviations are considerable in cases of higher volume fractions and shorter CNT lengths. This suggests that semi-empirical models struggle to accurately capture multi-directional load transfer mechanisms at higher reinforcement levels. In contrast, FEA incorporates these mechanisms through its simulation of localized stress and strain distributions within the RVE, leading to a more nuanced prediction of material behavior.

TABLE XI. RANGES OF PERCENTAGE INCREASE IN TRANSVERSE STIFFNESS FOR THE DIFFERENT MODELS

E_f/E_m	**FEA**	**(19)**	**(15)**
4.76	2% - 7%	2.4% - 9.5%	5.1% - 19.6%
7.69	2.1% - 8.8%	2.7% -10.6%	6.4% - 24.7%
14.29	4.9% - 10.7%	2.9% - 11.4%	

Figure 3 presents the range of percentage increases in transverse stiffness for different models (FEA, (15), and (19)). FEA (blue) predicts modest improvements with ranges between 2% and 7% at low E_f/E_m and up to 11% at higher ratios. Furthermore (19) (green) provides slightly wider ranges than the FEA model, extending to 11.4% at the highest ratio, while (15) (red) predicts much larger increases (5%–25%), but it is absent for the highest ratio (E_f/E_m = 14.29). This comparison shows that (15) predicts significantly greater transverse stiffness enhancement than (19) and FEA, while remaining in closer agreement. The observed trends in transverse modulus improvement are likely applicable to other material classes, including polymer-based matrices. The flexibility and lightweight nature of polymers, coupled with the stiffness enhancements provided by CNTs, could enable the

development of advanced composite materials for biomedical and sports equipment applications.

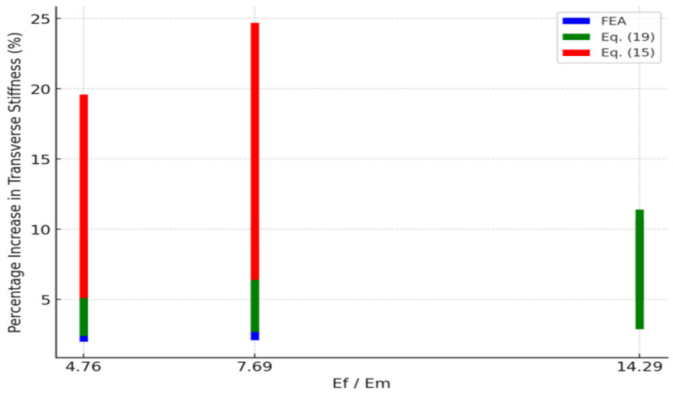

Fig. 3. Ranges of percentage increase in transverse stiffness for different models.

C. Shear Modulus

Tables XII-XIV display the FEA results for the shear modulus of the three fiber-to-matrix modulus ratios (G_f/G_m): 6.1%, 10.42%, and 19.23%. In general, the shear modulus of the composite material is greater than that of the matrix material. Shear decreases with increasing fiber length (L_{CNT}) and increases with increasing volume fraction (V_f). The greatest increase in composite shear modulus, 18.3%, was obtained with an L_{CNT} of 3 nm and a V_f of 11% for a chiral aluminum-based matrix composite structure. The chiral structure shows relatively higher Gf/Gm ratios for 10.42% and 19.23%, while the zigzag structure shows higher values for 6.1%. The superior performance of zigzag CNTs is explained by their atomic arrangement and shear stress transfer efficiency. Table XV presents the range of increases in shear modulus obtained by FEA, together with the values obtained by documented numerical equations. Most of the FE results (two-thirds) are lower than the values of both (16) and (20) by 0.1%-0.5%, while the remaining results are lower than the value of (16). The results of (16) are consistently higher than those of (20).

TABLE XII. SHEAR MODULUS RATIO (G_C/G_M=6.1)

			Armchair (5, 5)			**Zigzag (5, 0)**			**Chiral (5, 10)**		
			L_{CNT} =3	L_{CNT} =5	L_{CNT} =8	L_{CNT} =3	L_{CNT} =5	L_{CNT} =8	L_{CNT} =3	L_{CNT} =5	L_{CNT} =8
Volume fraction (%)	0.03	FEA	1.028	1.023	1.010	1.030	1.024	1.010	1.023	1.016	1.007
		(20)	1.026	1.026	1.026	1.026	1.026	1.026	1.026	1.026	1.026
		(16)	1.044	1.044	1.044	1.044	1.044	1.044	1.044	1.044	1.044
	0.07	FEA	1.068	1.059	1.021	1.076	1.062	1.022	1.059	1.040	1.017
		(20)	1.062	1.062	1.062	1.062	1.062	1.062	1.062	1.062	1.062
		(16)	1.106	1.106	1.106	1.106	1.106	1.106	1.106	1.106	1.106
	0.11	FEA	1.112	1.099	1.034	1.129	1.107	1.034	1.103	1.066	1.027
		(20)	1.101	1.101	1.101	1.101	1.101	1.101	1.101	1.101	1.101
		(16)	1.172	1.172	1.172	1.172	1.172	1.172	1.172	1.172	1.172

TABLE XIII. SHEAR MODULUS RATIO (G_C/G_M=10.42)

			Armchair (5, 5)			**Zigzag (5, 0)**			**Chiral (5, 10)**		
			L_{CNT} =3	L_{CNT} =5	L_{CNT} =8	L_{CNT} =3	L_{CNT} =5	L_{CNT} =8	L_{CNT} =3	L_{CNT} =5	L_{CNT} =8
Volume fraction (%)	0.03	FEA	1.029	1.022	1.010	1.031	1.025	1.010	1.031	1.023	1.013
		(20)	1.028	1.028	1.028	1.028	1.028	1.028	1.028	1.028	1.028
		(16)	1.051	1.051	1.051	1.051	1.051	1.051	1.051	1.051	1.051
	0.07	FEA	1.081	1.056	1.023	1.067	1.057	1.025	1.082	1.056	1.023
		(20)	1.068	1.068	1.068	1.068	1.068	1.068	1.068	1.068	1.068
		(16)	1.123	1.123	1.123	1.123	1.123	1.123	1.123	1.123	1.123
	0.11	FEA	1.146	1.092	1.036	1.108	1.094	1.038	1.144	1.094	1.035
		(20)	1.110	1.110	1.110	1.110	1.110	1.110	1.110	1.110	1.110
		(16)	1.200	1.200	1.200	1.200	1.200	1.200	1.200	1.200	1.200

TABLE XIV. SHEAR MODULUS RATIO (G_C/G_M=19.23)

			Armchair (5, 5)			**Zigzag (5, 0)**			**Chiral (5, 10)**		
			L_{CNT} =3	L_{CNT} =5	L_{CNT} =8	L_{CNT} =3	L_{CNT} =5	L_{CNT} =8	L_{CNT} =3	L_{CNT} =5	L_{CNT} =8
Volume fraction (%)	0.03	FEA	1.042	1.031	1.012	1.042	1.031	1.012	1.046	1.035	1.015
		(20)	1.029	1.029	1.029	1.029	1.029	1.029	1.029	1.029	1.029
		(16)	1.056	1.056	1.056	1.056	1.056	1.056	1.056	1.056	1.056
	0.07	FEA	1.087	1.058	1.025	1.073	1.050	1.019	1.104	1.069	1.029
		(20)	1.071	1.071	1.071	1.071	1.071	1.071	1.071	1.071	1.071
		(16)	1.135	1.135	1.135	1.135	1.135	1.135	1.135	1.135	1.135
	0.11	FEA	1.146	1.096	1.038	1.121	1.079	1.031	1.183	1.113	1.046
		(20)	1.116	1.116	1.116	1.116	1.116	1.116	1.116	1.116	1.116
		(16)	1.220	1.220	1.220	1.220	1.220	1.220	1.220	1.220	1.220

Figure 4 presents the percentage increase range in shear modulus for different models (FEA, (16), and (20), at various G_f/G_m values. The plot shows the range of the predicted percentage increases in shear modulus. FEA (blue) gives the lowest lower-bound values and moderate upper bounds. Furthermore (20) (green) predicts narrow ranges, with modest increases, while, (16) (red) shows the highest ranges, with higher lower bounds and maximum predictions compared to the other models. This comparison exhibits the significant impact of the modeling choices on predicted shear modulus enhancement.

Figure 5 depicts the variation in the predicted transverse stiffness increase by FEA and analytical equations for different fiber-to-matrix modulus ratios (E_f/E_m). Each subplot shows the stiffness range as vertical error bars, enabling a direct comparison between the numerical and analytical models. The plots reveal that while FEA predictions generally are within the analytical ranges, the equations tend to overestimate stiffness at higher fiber-to-matrix modulus ratios, resulting in wider predictions. The higher sensitivity of shear properties to interface strength and CNT aspect ratio leads to variations in the results.

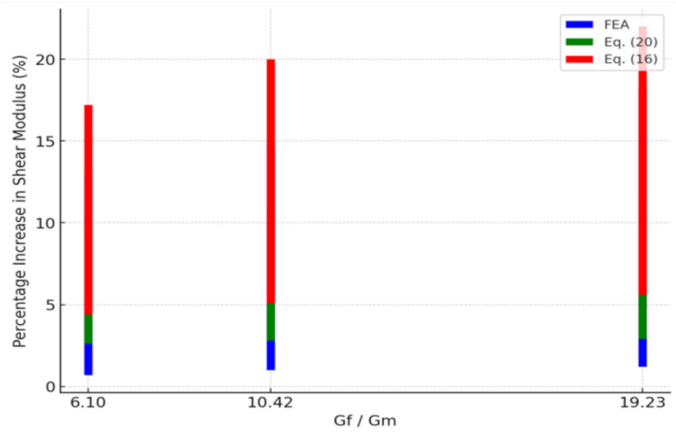

Fig. 4. Ranges of percentage increase in shear modulus for different modes.

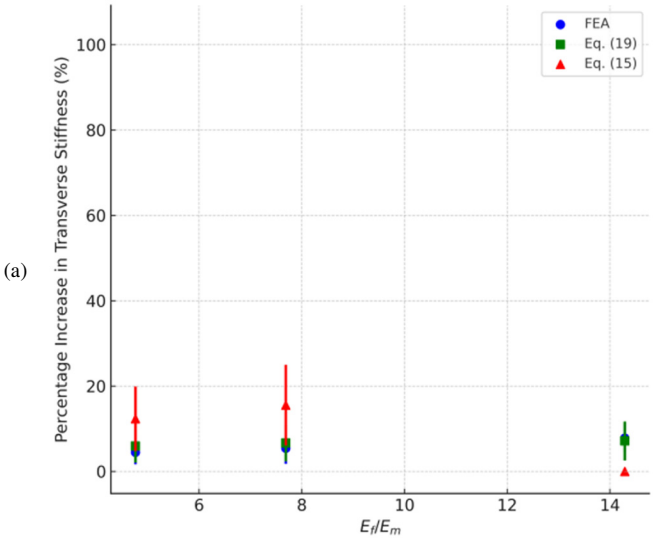

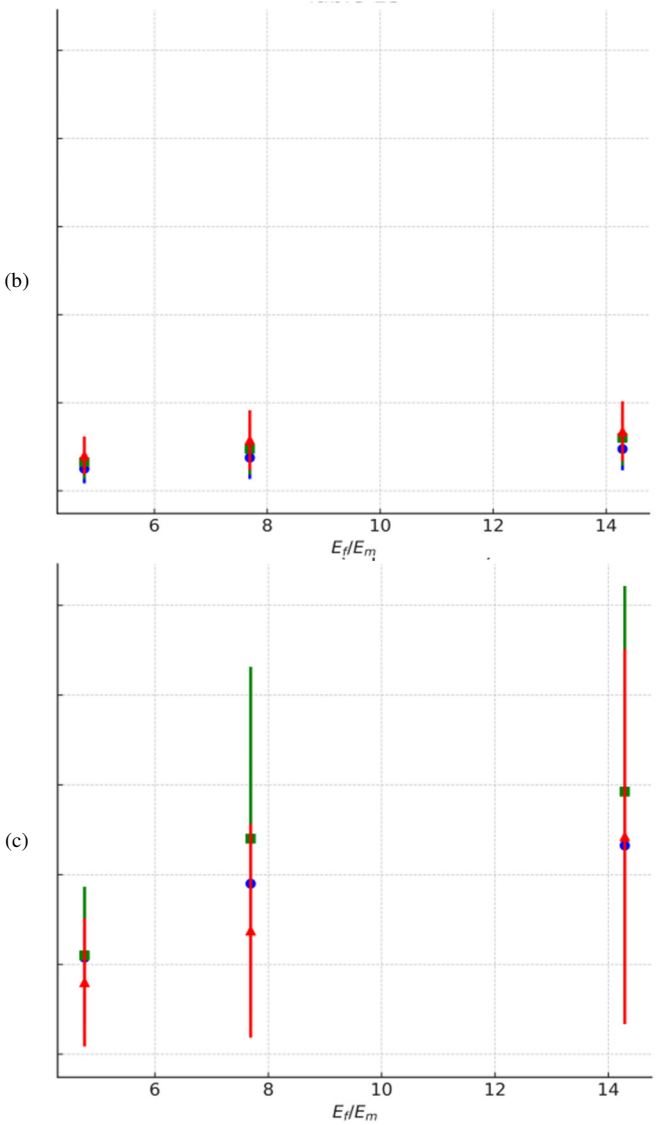

Fig. 5. Comparison of percentage increase in transverse stiffness across the three models: (a) Table XI, (b) Table XV, (c) new data.

While FEA directly simulates these interfacial interactions, semi-empirical models assume uniform load transfer, which can underestimate or overestimate the shear response. This underscores the importance of considering interface quality and CNT alignment when validating FEA results with empirical models.

VI. CONCLUSIONS

This study evaluated the mechanical performance of Carbon Nanotube (CNT)-reinforced Metal Matrix Composites (MMCs) using a combined Finite Element Analysis (FEA) and semi-empirical modeling approach. The results showed that the chirality, volume fraction, and fiber length of CNTs strongly affect stiffness. Zigzag CNTs were found to exceed the performance of armchair and chiral forms, with composites containing 11% volume fraction of zigzag CNTs and 8 nm fiber length exhibiting stiffness improvements of up to 76% in aluminum matrices. This validates the use of FEA to provide

detailed microstructural insights and semi-empirical models to efficiently predict mechanical properties. These findings offer design guidelines for manufacturing CNT-reinforced composites and reveal the necessity of refining semi-empirical models to more accurately capture chirality and interfacial effects. Future work should include dynamic property evaluation and the application of CNTs in ceramics and polymers, supported by multiscale modeling to bridge the gap between theoretical and experimental studies.

ACKNOWLEDGMENT

The author is thankful to the Deanship of Graduate Studies and Scientific Research at the University of Bisha for supporting this work through the Fast-Track Research Support Program.

The author also, expresses gratitude to Professor Saad Muhammad Suleiman and Dr. Gehad J. Suleiman for their valuable contributions and insightful feedback

REFERENCES

[1] J. Li *et al.*, "Multi-modal piezoresistive sensor based on cotton fiber aerogel/PPy for sound detection and respiratory monitoring," *Composites Science and Technology*, vol. 235, Apr. 2023, Art. no. 109953, https://doi.org/10.1016/j.compscitech.2023.109953.

[2] A. Esmaeili, C. Sbarufatti, A. Jiménez-Suárez, A. Ureña, and A. M. S. Hamouda, "A comparative study of the incorporation effect of SWCNT-OH and DWCNT with varied microstructural defects on tensile and impact strengths of epoxy based nanocomposite," *Journal of Polymer Research*, vol. 27, no. 6, May 2020, Art. no. 152, https://doi.org/10.1007/s10965-020-02135-z.

[3] K. J. Hughes *et al.*, "Review of Carbon Nanotube Research and Development: Materials and Emerging Applications," *ACS Applied Nano Materials*, vol. 7, no. 16, pp. 18695–18713, Aug. 2024, https://doi.org/10.1021/acsanm.4c02721.

[4] A. Yahyazadeh, S. Nanda, and A. K. Dalai, "Carbon Nanotubes: A Review of Synthesis Methods and Applications," *Reactions*, vol. 5, no. 3, pp. 429–451, Sept. 2024, https://doi.org/10.3390/reactions5030022.

[5] N. M. Nurazzi *et al.*, "Mechanical Performance and Applications of CNTs Reinforced Polymer Composites—A Review," *Nanomaterials*, vol. 11, no. 9, Sept. 2021, Art. no. 2186, https://doi.org/10.3390/nano11092186.

[6] S. Nguyen *et al.*, "Synthesis and characterization of hierarchical suspended carbon fiber structures decorated with carbon nanotubes," *Journal of Materials Science*, vol. 59, no. 7, pp. 2893–2906, Feb. 2024, https://doi.org/10.1007/s10853-024-09359-0.

[7] S. D. Müzel, E. P. Bonhin, N. M. Guimarães, and E. S. Guidi, "Application of the Finite Element Method in the Analysis of Composite Materials: A Review," *Polymers*, vol. 12, no. 4, Apr. 2020, Art. no. 818, https://doi.org/10.3390/polym12040818.

[8] M. Chwał and A. Muc, "FEM micromechanical modeling of nanocomposites with carbon nanotubes," *Reviews on Advanced Materials Science*, vol. 60, no. 1, pp. 342–351, Jan. 2021, https://doi.org/10.1515/rams-2021-0027.

[9] Í. Carneiro and S. Simões, "Strengthening Mechanisms in Carbon Nanotubes Reinforced Metal Matrix Composites: A Review," *Metals*, vol. 11, no. 10, Oct. 2021, Art. no. 1613, https://doi.org/10.3390/met11101613.

[10] M. R. Morovvati, B. Mollaei-Dariani, A. Lalehpour, and D. Toghraie, "Fabrication and finite element simulation of aluminum/carbon nanotubes sheet reinforced with Thermal Chemical Vapor Deposition (TCVD)," *Journal of Materials Research and Technology*, vol. 23, pp. 1887–1902, Mar. 2023, https://doi.org/10.1016/j.jmrt.2023.01.134.

[11] X. Nie and A. Bahrami, "Effect of carbon nanotubes on mechanical properties of aluminum matrix composites: A review," *Science and Engineering of Composite Materials*, vol. 31, no. 1, Jan. 2024, https://doi.org/10.1515/secm-2024-0009.

[12] M. S. Dresselhaus, G. Dresselhaus, and P. Avouris, Eds., *Carbon Nanotubes*, vol. 80. Berlin, Heidelberg: Springer, 2001.

[13] A. Chiminelli *et al.*, "Modeling Carbon-Based Nanomaterials (CNMs) and Derived Composites and Devices," *Sensors*, vol. 24, no. 23, Jan. 2024, Art. no. 7665, https://doi.org/10.3390/s24237665.

[14] T. Subhani, "Microstructure and Mechanical Properties of Carbon Fiber Phenolic MatrixComposites containing Carbon Nanotubes and Silicon Carbide," *Engineering, Technology & Applied Science Research*, vol. 14, no. 2, pp. 13637–13642, Apr. 2024, https://doi.org/10.48084/etasr.7070.

[15] E. W. Fenta and B. A. Mebratie, "Advancements in carbon nanotube-polymer composites: Enhancing properties and applications through advanced manufacturing techniques," *Heliyon*, vol. 10, no. 16, p. e36490, Aug. 2024, https://doi.org/10.1016/j.heliyon.2024.e36490.

[16] S. Zecchi *et al.*, "A Concise Review of Recent Advancements in Carbon Nanotubes for Aerospace Applications," *Micromachines*, vol. 16, no. 1, Jan. 2025, Art. no. 53, https://doi.org/10.3390/mi16010053.

[17] D. Bakošová and A. Bakošová, "Testing of Rubber Composites Reinforced with Carbon Nanotubes," *Polymers*, vol. 14, no. 15, Jan. 2022, Art. no. 3039, https://doi.org/10.3390/polym14153039.

[18] E. J. Barbero, *Finite Element Analysis of Composite Materials Using ANSYS*, 2nd ed. Boca Raton, Fl, USA: CRC Press, 2013.

[19] S. Zhu, S. Wu, Y. Fu, and S. Guo, "Prediction of particle-reinforced composite material properties based on an improved Halpin–Tsai model," *AIP Advances*, vol. 14, no. 4, Apr. 2024, Art. no. 045339, https://doi.org/10.1063/5.0206774.

[20] H.-H. Lee, *Finite Element Simulations with ANSYS Workbench 2021: Theory, Applications, Case Studies*, 1st ed. Boca Raton, Fl, USA: SDC Publications, 2021.

[21] S. M. A. K. Mohammed and D. L. Chen, "Carbon Nanotube-Reinforced Aluminum Matrix Composites," *Advanced Engineering Materials*, vol. 22, no. 4, 2020, Art. no. 1901176, https://doi.org/10.1002/adem.201901176.

[22] R. Sahu, D. Harursampath, and S. A. Ponnusami, "Mechanical behaviour of carbon nanotube composites: A review of various modelling techniques," *Journal of Composite Materials*, vol. 58, no. 6, pp. 791–825, Mar. 2024, https://doi.org/10.1177/00219983231213967.

[23] R. Sahu, S. A. Ponnusami, C. Weimer, and D. Harursampath, "Interface engineering of carbon fiber composites using CNT: A review," *Polymer Composites*, vol. 45, no. 1, pp. 9–42, 2024, https://doi.org/10.1002/pc.27772.

[24] A. Kumar, K. Sharma, and A. R. Dixit, "A review on the mechanical properties of polymer composites reinforced by carbon nanotubes and graphene," *Carbon Letters*, vol. 31, no. 2, pp. 149–165, Apr. 2021, https://doi.org/10.1007/s42823-020-00161-x.

[25] D. G. Papageorgiou, Z. Li, M. Liu, I. A. Kinloch, and R. J. Young, "Mechanisms of mechanical reinforcement by graphene and carbon nanotubes in polymer nanocomposites," *Nanoscale*, vol. 12, no. 4, pp. 2228–2267, Jan. 2020, https://doi.org/10.1039/C9NR06952F.

[26] R. Teixeira-Santos, M. Gomes, L. C. Gomes, and F. J. Mergulhão, "Antimicrobial and anti-adhesive properties of carbon nanotube-based surfaces for medical applications: a systematic review," *iScience*, vol. 24, no. 1, Jan. 2021, Art. no. 102001, https://doi.org/10.1016/j.isci.2020.102001.

[27] B. D. Agarwal, L. J. Broutman, and K. Chandrashekhara, *Analysis and Performance of Fiber Composites*, 3rd ed. Hoboken, NJ, USA: John Wiley & Sons, 2006.

[28] R. K. Mishra, K. Verma, and D. sethi singh, "Defect engineering in nanomaterials: Impact, challenges, and applications," *Smart Materials in Manufacturing*, vol. 2, Jan. 2024, Art. no. 100052, https://doi.org/10.1016/j.smmf.2024.100052.

[29] A. Agarwal, S. Garg, H. Wassan, P. Joshi, and R. K. Tyagi, "Investigation of mechanical behavior of carbon nanotube-reinforced magnesium composite," *International Journal of Computational Materials Science and Engineering*, vol. 12, no. 01, Mar. 2023, Art. no. 2250016, https://doi.org/10.1142/S2047684122500166.

[30] S. Saurabh, N. D. Chakladar, A. Deb, and N. K. Sharma, "Multiscale modeling of multiwalled carbon nanotube-reinforced polymer matrix nanocomposites and experimental validation," *Polymer Composites*, vol. 46, no. 8, pp. 7422–7445, 2025, https://doi.org/10.1002/pc.29439.

[31] Y. Miao, Q. Chen, Y. Li, D. Zhuo, and R. Wang, "Tribological properties of carbon nanotube/polymer composites:A mini-review," *Frontiers in Materials*, vol. 10, Jan. 2023, https://doi.org/10.3389/fmats.2023.1129676.

[32] A. Agarwal, A. Nieto, D. Lahiri, A. Bisht, and S. R. Bakshi, *Carbon nanotubes: reinforced metal matrix composites*, 2nd ed. Abingdon, Oxon, UK: CRC Press, 2021.

[33] M. H. Ali, R. I. Rubel, M. H. Ali, and R. I. Rubel, "A comparative review of Mg/CNTs and Al/CNTs composite to explore the prospect of bimetallic Mg-Al/CNTs composites," *AIMS Materials Science*, vol. 7, no. 3, pp. 217–243, 2020, https://doi.org/10.3934/matersci.2020.3.217.

[34] H. Purnomo *et al.*, "Advanced Composite Materials Development for Aerospace Applications: The Key Role of MWCNTs in Performance Improvement," *Engineering, Technology & Applied Science Research*, vol. 15, no. 3, pp. 23877–23885, June 2025, https://doi.org/10.48084/etasr.11051.

[35] X. Gao *et al.*, "Recent advances in carbon-based nanomaterials for multivalent-ion hybrid capacitors: a review," *Energy & Environmental Science*, vol. 16, no. 4, pp. 1364–1383, Apr. 2023, https://doi.org/10.1039/D2EE03719J.